

Ground-state OH observations towards NGC 6334

K. J. Brooks¹★ and J. B. Whiteoak²

¹ Department of Physics, University of New South Wales, Sydney 2052, NSW Australia

² Australia Telescope National Facility, CSIRO, PO Box 76, Epping 2121, NSW Australia

9 November 2018

ABSTRACT

We have made observations of the four hyperfine transitions of the $^2\Pi_{3/2}$, $J=3/2$ ground state of OH at 1612, 1665, 1667 and 1720 MHz and the related 1.6-GHz continuum emission, towards NGC 6334 using the Australia Telescope Compact Array. The observations covered all the major radio continuum concentrations aligned along the axis of NGC 6334 (V, A to F). We have detected seven OH masers plus a possible faint eighth maser; two of these masers are located towards NGC 6334-A. Absorption at 1665 and 1667 MHz was detected towards almost all the continuum distribution. All transitions showed non-LTE behaviour. The 1667-/1665-MHz intensity ratios ranged from 1.0 to 1.2, significantly less than their LTE value of 1.8. The results of the OH ‘Sum Rule’ suggest that this discrepancy cannot be explained solely by high optical depths. The 1612- and 1720-MHz line-profiles showed conjugate behaviour whereby one line was in absorption and the other in emission. In addition, the profiles commonly showed a flip from absorption to emission and vice versa, which has been interpreted as a density gradient. The OH line-to-continuum distribution, optical depth and velocity trends are consistent with a bar-like shape for the molecular gas which wraps around the continuum emission.

Key words:

line profiles - masers - H II regions — ISM: clouds, kinematics and dynamics — stars: formation

1 INTRODUCTION

NGC 6334 is a prominent H II region/molecular cloud complex located in the Sagittarius arm of the Milky Way at a photometric distance of 1.7 kpc (Neckel 1978) (1pc \approx 2 arcmin). The complex contains several recent and current star-forming sites which are embedded in an elongated giant molecular cloud (GMC) extending over about 45 arcmin (Dickel, Dickel, & Wilson 1977, Kraemer & Jackson 1999).

Far-infrared observations at wavelengths 80–250 microns by McBreen et al. (1979) revealed six strong continuum concentrations, the peaks of which are designated FIR-I to FIR-VI. Sources I to V are present along a ridge of extended continuum emission which runs northeast–southwest, parallel to the plane of our Galaxy, while the weak, extended source VI is situated further south. Observations at 4.9 GHz by Rodríguez, Cantó, & Moran (1982) yielded six continuum concentrations also located along the ridge. Designated A to F, some are coincident with the far-

infrared concentrations. The continuum ridge is coincident with a dark dust lane seen at optical wavelengths (e.g Gardner & Whiteoak 1975). The dust lane appears to be obscuring the optical ionized distribution, suggesting that it is overlying the nebulosity. The radio continuum concentrations have been individually observed in several projects (see discussion in Section 3.1). The results show that most of them have associated outflows, sites of maser emission, or embedded protostars, all indicative of very active sites of star formation.

To further investigate the physical conditions of the NGC 6334 complex, we have carried out a series of observations of the 1612-, 1665-, 1667-, and 1720-MHz hyperfine transitions of the $^2\Pi_{3/2}$, $J=3/2$ ground state of OH using the Australia Telescope Compact Array (ATCA)[†]. These four transitions are valuable in investigations of molecular clouds because they can exhibit extended emission and absorption and maser emission.

★ Current institute: European Southern Observatory, Casilla 19001, Santiago 19, Chile (kbrooks@eso.org)

[†] The Australia Telescope is funded by the Commonwealth of Australia for operation as a National Facility managed by CSIRO.

A direct result of the statistical weights and transition probabilities of the ‘main lines’ (at 1665 and 1667 MHz) and ‘satellite lines’ (at 1612 and 1720 MHz) is that, under conditions of local thermodynamic equilibrium (LTE), their optical depths, τ_{1612} , τ_{1665} , τ_{1667} , τ_{1720} , are in the ratio 1:5:9:1. Previous studies of OH have shown that both the main-line and satellite-line intensities often show non-LTE ratios. The satellite lines can also exhibit a conjugate-type behaviour whereby emission of one line is accompanied by absorption of the other. This behaviour is explained in detail by Elitzur (1992) and references therein. The satellite-line behaviour can be used as a diagnostic for the type of OH excitation process taking place in the region and may also provide density constraints. For example, radiative excitation at high densities can produce 1612-MHz emission but collisional excitation at low temperatures can lead to 1720-MHz emission (Elitzur 1992).

The ratios of the optical depths of the four transitions give

$$\tau_{1612} + \tau_{1720} = \frac{\tau_{1665}}{5} + \frac{\tau_{1667}}{9}. \quad (1)$$

This relationship is commonly termed the ‘Sum Rule’ (e.g. Rogers & Barrett 1967) and can be used to obtain optical depth measurements even in cases where LTE is not satisfied. For low optical depths and an extended continuum emission with a flat spectrum the Sum Rule becomes

$$T_{1612} + T_{1720} = \frac{T_{1665}}{5} + \frac{T_{1667}}{9}, \quad (2)$$

where T_{line} is the line temperature of the transition.

2 OBSERVATIONS

The ATCA observations were carried out with six different array configurations between 1994 September and 1995 August. Details of the instrument are given by Frater & Brooks (1992). The antenna spacings ranged from 30 m to 6 km. All sets of observations were made with the correlator configured to 2048 frequency channels over a bandwidth of 4 MHz, providing a velocity resolution of 0.42 km s^{-1} . Two orthogonal linear polarisations were observed and then later averaged together. The observations were made using standard procedures, cycling through frequencies centred on 1666, 1720 and 1612 MHz. The 1665- and 1667-MHz lines were both included in the band centred at 1666 MHz. Observations of PKS 1740-517 were used for phase and bandpass calibration. Flux-density calibration was provided by observing PKS 1934-638 (adopted as the ATCA primary calibrator), for which flux densities of 14.3, 14.2, 14.0 Jy were adopted at 1612, 1666 and 1720 MHz respectively.

At 1.6 GHz, the half-power primary beamsize of the ATCA is 30 arcmin. For observations centred on RA(B1950) = $17^h 17^m 10^s$, Dec(B1950) = $-35^\circ 49' 00''$, the half-power primary beam covered all the major continuum concentrations along the ridge of NGC 6334.

The correlated spectral outputs from pairs of ATCA antennae were processed using a package based on the Astronomical Image Processing System (AIPS) produced by the US National Radio Astronomy Observatory. The continuum emission was subtracted from each spectral-line dataset and then combined into a single continuum dataset. For all four

spectral-line datasets, the frequency scale was converted to a velocity scale with respect to the local standard of rest (LSR). Amplitude and phase self-calibration were applied to the 1665-, 1667- and 1720-MHz datasets, all of which contained strong maser emission. Strong residuals remained in the main-line channel maps ($\sim 50 \text{ mJy beam}^{-1}$ for the images near the central velocities of the masers) because the intensities of the two masers both varied on time scales of a few months, producing different values measured for each array-configuration.

Image analysis was carried out using MIRIAD (Sault, Teuben, & Wright 1995) and KARMA (Gooch 1996). Uniform and natural weighting were used for both the continuum data and each channel of the line data. Multi-frequency synthesis (Sault & Wieringa 1994) was also adopted for the continuum data. Each image was deconvolved using the CLEAN algorithm of Steer, Dewdney, & Ito (1984) and restored with diffraction-limited beams of $4.6 \times 7.2 \text{ arcsec}^2$ (uniform weighting) and $25.8 \times 19.6 \text{ arcsec}^2$ (natural weighting). Each image was also corrected for the primary beam gain pattern of the individual antennas. The uniform-weighted line images, with a velocity resolution of 0.42 km s^{-1} , were used to investigate maser emission and the natural-weighted line images, Hanning smoothed to a velocity resolution of 0.7 km s^{-1} , were used to investigate the extended OH emission.

3 RESULTS

3.1 1.6-GHz Continuum distribution

Fig. 1 shows the natural-weighted 1.6-GHz continuum image with an rms noise level of $0.009 \text{ Jy beam}^{-1}$. The main emission concentrations are labelled using the nomenclature of Rodríguez et al. (1982) and McBreen et al. (1979) and their positions and fluxes are described in Table 1. The position of the far-infrared source NGC 6334-I(N) is marked with a cross (see Section 3.1.6). The overall structure of NGC 6334-A to -F is similar to that derived by Rodríguez et al. (1982, 1988) at 4.9 GHz, and De Pree et al. (1995) at 8.3 GHz. Continuum emission at 1.6-GHz was also detected towards NGC 6334-V and as a weak source south of NGC 6334-D (NGC 6334-D(S)). All of the concentrations are superimposed on faint emission which extends northwest from the dark dust lane. This faint emission, and also the two faint semi-circular emission regions near the southern boundary of Fig. 1, follow the optical and infrared distributions.

The uniform-weighted 1.6-GHz continuum image has an rms noise level of $0.02 \text{ Jy beam}^{-1}$. For this image, the main continuum concentrations listed in Table 1 are discussed separately, with the exception of NGC 6334-D(S). This source was not detected in the uniform-weighted image, which suggests it may be a diffuse source of the order of 20 arcsec in diameter.

3.1.1 NGC 6334-V

This source was first detected by McBreen et al. (1979) and has a supersonic bipolar outflow that is associated with shock-excited molecular hydrogen gas (Fischer et al. 1982, 1985, Straw & Hyland 1989a, Kraemer & Jackson 1999).

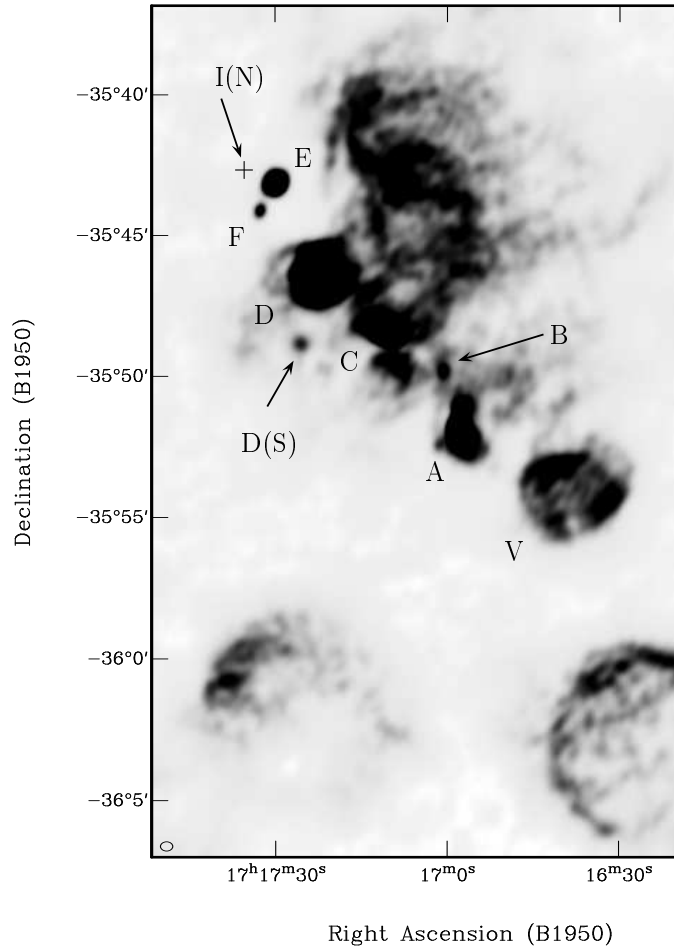


Figure 1. NGC 6334: 1.6-GHz continuum emission imaged with a 25.8×19.6 arcsec 2 beam, shown bottom left

Table 1. 1.6-GHz continuum parameters measured from Fig. 1.

Region	Peak position ^a		Peak flux	Integrated flux	Velocity
	RA(B1950)	DEC(B1950)	(Jy beam $^{-1}$)	(Jy)	(km s $^{-1}$)
NGC 6334-V	17 ^h 16 ^m 39 ^s 50	-35°53'05"9	0.458 ± 0.009	11 ± 2	
NGC 6334-A	17 16 57.80	-35 51 43.9	4.128 ± 0.009	12.9 ± 0.7	-0.1 ± 0.2 ^b
NGC 6334-B	17 17 00.58	-35 49 47.2	0.417 ± 0.009	0.417 ± 0.009	
NGC 6334-C	17 17 10.98	-35 48 27.0	2.295 ± 0.009	9.3 ± 0.3	-2.5 ± 0.3 ^c
NGC 6334-D	17 17 22.87	-35 46 18.7	1.818 ± 0.009	23 ± 2	-2.5 ± 0.3 ^c
NGC 6334-D(S)	17 17 25.52	-35 48 58.9	0.266 ± 0.009	0.266 ± 0.009	
NGC 6334-E	17 17 29.61	-35 43 06.6	1.636 ± 0.009	3.9 ± 0.1	
NGC 6334-F	17 17 32.53	-35 44 06.9	0.433 ± 0.009	0.433 ± 0.009	-6.1 ± 0.3 ^b

^a With a positional uncertainty of 1.5 arcsec

^b Taken from H76 α recombination line observations of De Pree et al. (1995)

^c Taken from H109 α recombination line observations of Reifenstein et al. (1970)

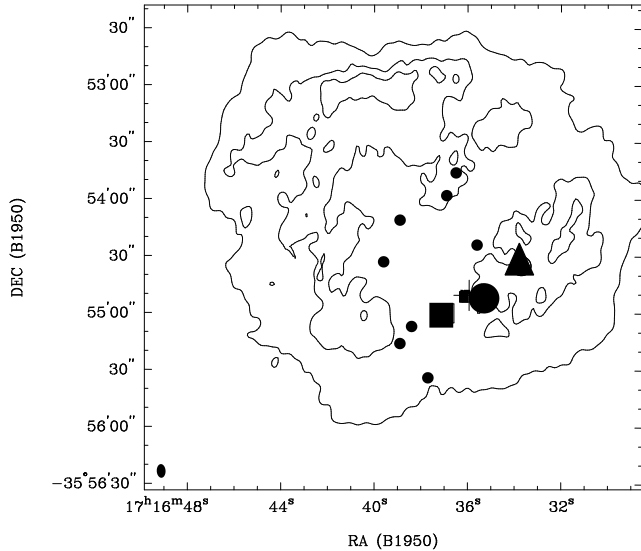


Figure 2. NGC 6334-V: 1.6-GHz continuum emission imaged with a 4.6×7.2 arcsec 2 beam, shown bottom left. The contour levels are 25, 40 and 50 mJy beam $^{-1}$. The other features shown and their positional uncertainties are: cross – OH maser ($\pm 0.^{\prime}1$); triangle – NH₃ maser ($\leq \pm 3.^{\prime\prime}$); small box – H₂O maser ($\pm 0.^{\prime}2$); large box – FIR-V ($\pm 30.^{\prime\prime}$); small circle – star formation sites ($\pm 4.^{\prime\prime}$); large circle – central protostar, IRS-24 ($\pm 4.^{\prime\prime}$).

Wolstencroft, Scarrott, & Warren-Smith (1987) have suggested that the outflow is powered by a protostar, designated IRS-24 by Straw, Hyland, & McGregor (1989). This protostar may also be triggering nearby sites of star formation. Kraemer & Jackson (1995) have detected shock-excited NH₃ maser emission at the edge of the outflow. OH and H₂O maser emission have also been detected (e.g. Forster & Caswell 1989; Caswell 1998). Jackson & Kraemer (1999) detected faint 8.485-GHz continuum emission counterparts to FIR-V which may be additional protostars.

Fig. 2 reveals that the faint 1.6-GHz continuum emission in this region has the morphology of a spherical shell with a diameter of about 3.5 arcmin. The shell is centred about 1 arcmin northeast of IRS-24 and parts of it have recently been detected by Jackson & Kraemer (1999) at 8.485 GHz. The source of ionization is not known.

3.1.2 NGC 6334-A

This component was first identified by Schraml & Mezger (1969). A bipolar morphology of the ionized gas was first detected by Harvey & Gatley (1983). The exciting star(s) of the region could be the infrared sources IRS-19 and/or IRS-20 (Straw, Hyland, & McGregor 1989), identified as two B-type stars (Harvey & Gatley 1983). The elongated morphology and velocity gradients of the ionized gas were interpreted as evidence of a confining molecular disk (Rodríguez, Cantó, & Moran 1988 and De Pree et al. 1995). Molecular-line observations by Kraemer et al. (1997) revealed a flattened, massive, rotating structure of molecular gas which extends 3 arcmin in the east–west direction (aligned perpendicular to the continuum emission) and is centred near the IRS objects. In addition, several small NH₃ emission clumps were detected within this molecular structure. One clump was

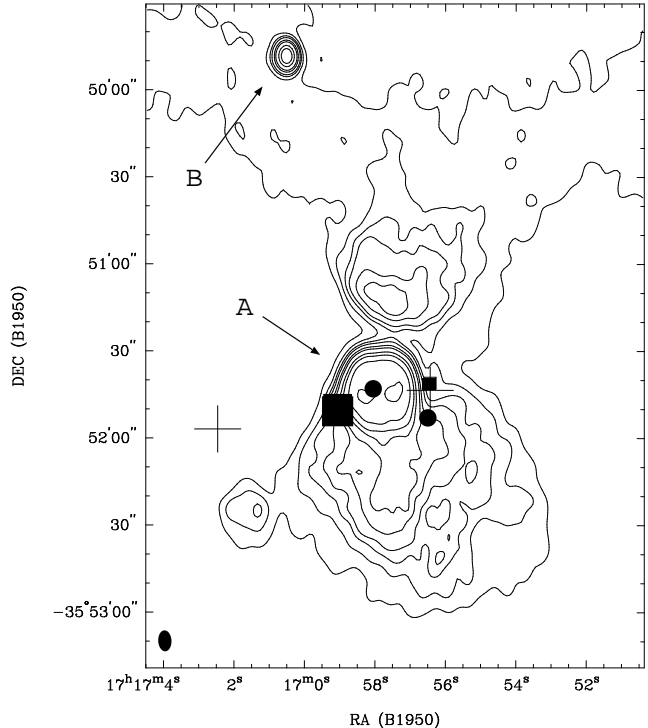


Figure 3. NGC 6334-A: 1.6-GHz continuum emission imaged with a 4.6×7.2 arcsec 2 beam, shown bottom left. The contour levels are 30, 40, 50, 60, 80, 100, 150, 200, 300 and 450 mJy beam $^{-1}$. The other sources shown and their positional uncertainties are: cross – OH masers ($\leq \pm 0.^{\prime}7$); small box – H₂O maser ($\pm 0.^{\prime}2$); large box – FIR-IV ($\pm 30.^{\prime\prime}$); circle – bright infrared sources, IRS-19 (left) and IRS-20 (right), (both $\pm 4.^{\prime\prime}$). The figure also shows NGC 6334-B, the compact northern source believed to be extragalactic – see Section 3.1.3.

found to be coincident with a site of H₂O maser emission detected by Rodríguez et al. (1988) and another with IRS-20. Kraemer et al. (1997) have suggested that these clumps are part of a protocluster of stars which is condensing from the massive molecular disk. Jackson & Kraemer (1999) have detected an unresolved 8.485-GHz continuum source at the location of IRS-20 which could be an optically thick H_{II} containing a star undergoing mass loss.

The 1.6-GHz continuum emission in Fig. 3 shows the same bipolar morphology seen at other wavelengths, in which faint northern and southern extended emission lobes extend out from a strong spherical shell. The lobes extend over 3 arcmin north–south and the continuum shell has a diameter of 30 arcsec. The structure of the lobes is well defined, with the extended emission narrowing at the northern edge of the central shell.

3.1.3 NGC 6334-B

Fig. 3 also shows the unresolved continuum emission of NGC 6334-B. The flux of this source at 1.6 GHz was found to be 0.48 Jy, similar to the values 0.4, 0.6, 0.4 Jy at 4.8, 8.3 and 14.7 GHz respectively, derived by De Pree et al. (1995). The source is superimposed on the faint, extended emission seen northwards of NGC 6334-A. It is believed to be a flat-spectrum extragalactic source and has been discussed by

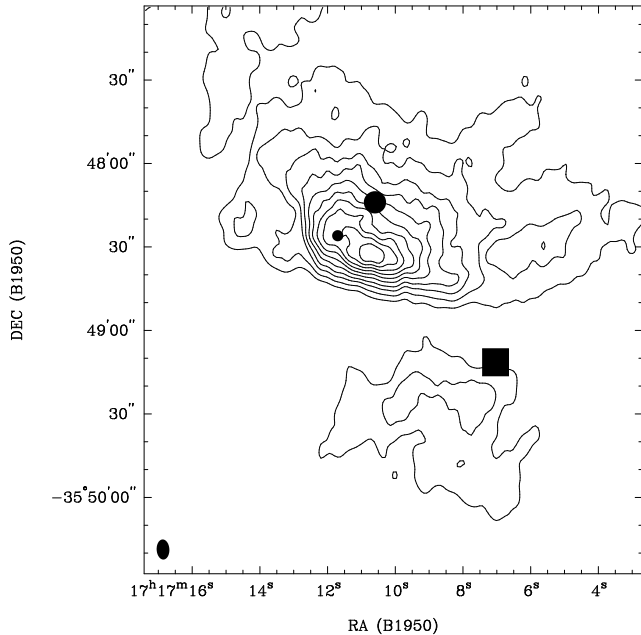


Figure 4. NGC 6334-C: 1.6-GHz continuum emission distribution imaged with a 4.6×7.2 arcsec 2 beam, shown bottom-left. The contour levels are 45, 60, 80, 100, 125, 150, 175, 200, 225 and 250 mJy beam $^{-1}$. The other sources shown and their positional uncertainties are: *large box* – FIR-III ($\pm 30''$); *large circle* – compact infrared source ($\pm 10''$); *small circle* – Br α line emission ($\pm 10''$).

Rodríguez et al. (1982) and Moran et al. (1990). They found a variation of intensity and angular size with wavelength which they explained in terms of scattering by the ionized gas of NGC 6334-A.

3.1.4 NGC 6334-C

This H α region was first discussed by Schraml & Mezger (1969). IRS-13 is believed to be responsible for the ionization of the region (Straw et al. 1989). FIR-III appears to be centred to the southwest of the main radio emission, even when its positional uncertainty of ± 30 arcsec is considered. Because of the relative diffuseness of the radio emission and lack of maser sources NGC 6334-C was thought to be one of the older areas of NGC 6334. However, Straw & Hyland (1989b) have detected a significant number of low-to-intermediate-mass pre-main-sequence objects in this region. Persi & Ferrari-Toniolo (1982) have detected a compact infrared source as well as Br α line emission towards an infrared peak that may be associated with an extreme young object.

The 1.6-GHz continuum emission (Fig. 4) is extended to the north but the southern edge is clearly compressed, in agreement with the observations by De Pree et al. (1995).

3.1.5 NGC 6334-D

This is another of the three H α components first discussed by Schraml & Mezger (1969). The presence of an intense arc of H α emission lying to the southeast of FIR-II led Straw & Hyland (1989a) to suggest that this region of the molecular cloud has been swept relatively clear of gas and dust by an

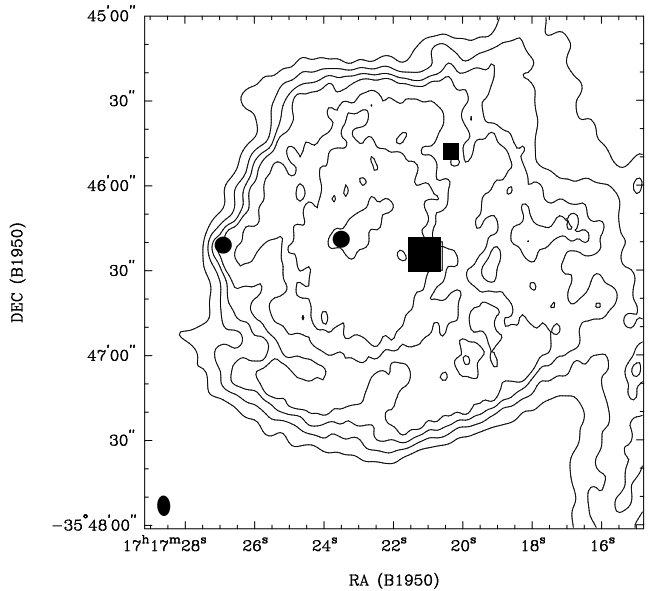


Figure 5. NGC 6334-D: 1.6-GHz continuum emission distribution imaged with a 4.6×7.2 arcsec 2 beam, shown bottom left. The contour levels are 30, 40, 50, 60, 80, 100 and 150 mJy beam $^{-1}$. The other sources shown and their positional uncertainties are: *small box* – H₂O maser ($\pm 20''$); *large box* – FIR-II ($\pm 30''$); *circle* – IRS-23 (left), IRS-24 (right), (all $\pm 4''$).

outflow responsible for the H α emission. As yet, no further observations have been made to confirm the presence of this outflow. Two possible candidates that may be powering the outflow are IRS-23, an early B-type star, and IRS-24, an O-type star thought to be also responsible for the continuum emission (Straw et al. 1989). Because of its extended, spherical continuum structure NGC 6334-D is thought to be one of the more evolved H α regions, although the region contains, in addition to the infrared objects already mentioned, a significant number of pre-main-sequence objects (Straw & Hyland 1989b) and H₂O maser emission (Moran & Rodríguez 1980).

Consistent with previous observations at higher frequencies, the 1.6-GHz continuum emission (Fig. 5) is spherical and featureless with a diameter of 2.5 arcmin. The arc of intense H α emission is along the south-eastern edge.

3.1.6 NGC 6334-E

NGC 6334-E was first detected by Rodríguez et al. (1982) as a spherical and featureless radio-continuum source. A cluster of B-type stars is thought to be responsible for the ionization (Tapia, Persi, & Roth 1996). To the northwest of it is the well-studied source NGC 6334-I(N). Its position is shown on Fig. 1. This source is the brightest 1-mm continuum source observed in NGC 6334 (Cheung et al. 1978). It is likely to be an active star-formation region in the early stages of evolution (see Tapia et al. 1996 and references therein).

The 1.6-GHz continuum emission of NGC 6334-E (Fig. 6) is consistent with an evolved spherical shell of diameter 40 arcsec. No continuum emission at 1.6 GHz was detected towards NGC 6334-I(N) to an upper limit of 9 mJy beam $^{-1}$.

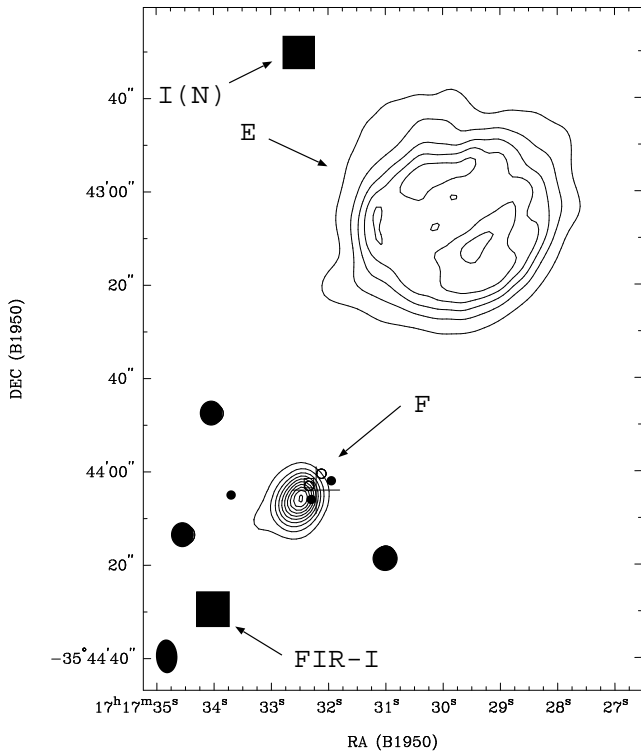


Figure 6. NGC 6334-E, -F: 1.6-GHz continuum emission distribution imaged with a 4.6×7.2 arcsec 2 beam, shown bottom left. The contour levels are 25, 50, 75, 100, 125, 150, 175, 200, 225, 250 mJy beam $^{-1}$. The other sources shown and their positional uncertainties are: cross – OH masers ($\pm 0''.1$); large circle – NH₃ masers ($\leq \pm 3''$); open small circle – CH₃OH masers ($\pm 0''.2$); open small box – H₂O maser ($\pm 0''.4$); large box – FIR-I ($\pm 30''$), I(N) ($\pm 0''.5$); small circle – IRS-3(left), IRS-1 (middle), IRS-2 (right), (all $\pm \leq 7''$). The H₂O maser and one CH₃OH maser are coincident.

3.1.7 NGC 6334-F

NGC 6334-F is an ultra-compact H II region that is optically obscured. It has been described as a ‘nozzle’ by Rodríguez et al. (1982). High-resolution continuum observations by Ellingsen, Norris, & McCulloch (1996) and De Pree et al. (1995) show evidence of compression on the north-eastern edge. FIR-I is located 30 arcsec to the southeast but in view of its positional uncertainty of 30 arcsec, may in reality be associated with the object. The excitation of the H II region is caused by IRS-1, most likely a massive star (Harvey & Gatley 1983). From recent thermal dust imaging by Persi et al. (1998) it appears that the circumstellar dust of IRS-1 is intermixed with the ionized gas associated with the H II region. A molecular bipolar outflow extends across the H II region in a northeast–southwest direction Bachiller & Cernicharo (1990). Sites of NH₃ maser emission (Kraemer & Jackson 1995) and shocked H₂ emission (Persi et al. 1996) occur at the ends of the outflow. A velocity gradient is also detected in the ionized gas (De Pree et al. 1995). It is still not clear if the outflow is powered by IRS-1 or a nearby infrared source, IRS-2 (Harvey & Gatley 1983). Maser sites for transitions of OH (e.g. Gaume & Mutel 1987; Caswell 1998), H₂O (e.g. Forster & Caswell 1989) and CH₃OH (e.g. Caswell 1997) are located towards or near the H II region.

The 1.6-GHz continuum emission is barely resolved in Fig. 6, revealing a slight extension in the southeast, north-west direction. The measured flux at 1.6 GHz was 0.43 Jy, consistent with the values of 0.59 measured at 8.5 GHz Ellingsen et al. (1996) and 0.4 and 0.1 Jy measured at 14.5 and 4.8 GHz respectively (De Pree et al. 1995).

3.2 OH maser emission

Seven OH masers were unambiguously detected. There is strong observational evidence to suggest that OH masers are linked to massive young stars and ultracompact H II regions even though the details of their pumping mechanism remain unclear (e.g. Elitzur 1992). All of the masers detected are located along the main continuum axis and are associated with three of the components discussed earlier. Their presence suggests that star formation is still occurring in these regions. Table 2 lists the peak intensity, velocity and position for each maser obtained from a 2-dimensional Gaussian fit to the peak emission. Fig. 7 shows the seven individual spectra.

The strongest OH masers are associated with NGC 6334-V and NGC 6334-F and are well documented from previous studies. We have obtained positional uncertainties of ± 0.1 arcsec. For NGC 6334-V our 1665- and 1667-MHz maser positions differ by 0.7 arcsec and their positions are coincident to within 0.3 arcsec of the previous detections by Caswell (1998) which have a positional error of ± 0.4 arcsec. It appears that the location of the two masers differ slightly. In contrast, for NGC 6334-F our 1665 and 1667 masers are coincident in position to within their positional errors and to within 0.3 arcsec of the respective positions measured by Caswell (1998). The 1720-MHz maser is offset in position from the main-line masers by 0.8 arcsec. Its position differs by 0.4 arcsec from the previous detection by Gaume & Mutel (1987) which has a positional error of ± 0.15 arcsec. A possible new detection of a faint 1612-MHz maser associated with NGC 6334-F is discussed in Section 3.3.3.

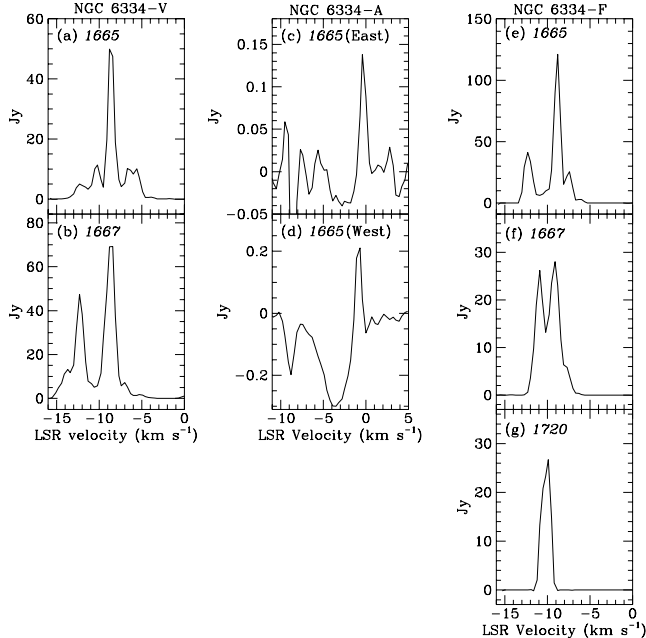
Two 1665-MHz masers were detected towards NGC 6334-A. In contrast to the other 1665-MHz masers which are bright and peaked near -8.7 km s $^{-1}$, these two masers are faint with single features at more positive velocities. One has a velocity of -0.8 km s $^{-1}$ and occurs at the western edge of the continuum peak (see Fig. 3). It is offset from the nearby H₂O maser by 2.7 (± 0.3) arcsec. The other OH maser is situated 1 arcmin east of the continuum shell and has a velocity of -0.3 km s $^{-1}$. It does not appear to be associated with any other detected features. The flattened molecular structure described in Section 3.1.2 extends out past this new maser site. If star formation is thought to be occurring within this structure then the maser may be pinpointing a new site of star formation.

3.3 Extended OH emission and absorption

The OH absorption profiles (see e.g. Fig. 9) reveal two molecular clouds located along the line of sight to NGC 6334, one with velocities extending from -15 to $+2$ km s $^{-1}$, the other with a well-defined velocity near $+6$ km s $^{-1}$. The more negative velocity absorption is confined towards NGC 6334 whereas the narrow absorption at $+6$ km s $^{-1}$ is also detected

Table 2. Parameters of the peak OH maser emission.

Region	OH line (MHz)	Peak position		Peak Intensity (Jy)	Velocity (km s ⁻¹)
		RA(B1950)	DEC(B1950)		
NGC 6334-V	1665	$17^h 16^m 35.94 \pm 0.08$	$-35^{\circ} 54' 51.2 \pm 0.1$	53.8 ± 0.9	-8.622 ± 0.007
	1667	$17^h 16^m 35.94 \pm 0.01$	$-35^{\circ} 54' 50.5 \pm 0.1$	72 ± 1	-8.7 ± 0.7
NGC 6334-A	1665	$17^h 16^m 56.43 \pm 0.03$	$-35^{\circ} 51' 43.6 \pm 0.3$	0.24 ± 1	-0.8 ± 1
	1665	$17^h 17^m 02.46 \pm 0.02$	$-35^{\circ} 51' 56.9 \pm 0.7$	0.14 ± 1	-0.3 ± 2
NGC 6334-F	1665	$17^h 17^m 32.22 \pm 0.01$	$-35^{\circ} 44' 04.0 \pm 0.1$	120.1 ± 0.9	-8.860 ± 0.003
	1667	$17^h 17^m 32.23 \pm 0.01$	$-35^{\circ} 44' 04.1 \pm 0.1$	28.1 ± 0.5	-8.94 ± 0.03
	1720	$17^h 17^m 32.23 \pm 0.01$	$-35^{\circ} 44' 04.8 \pm 0.1$	27.1 ± 0.7	-10.16 ± 0.02

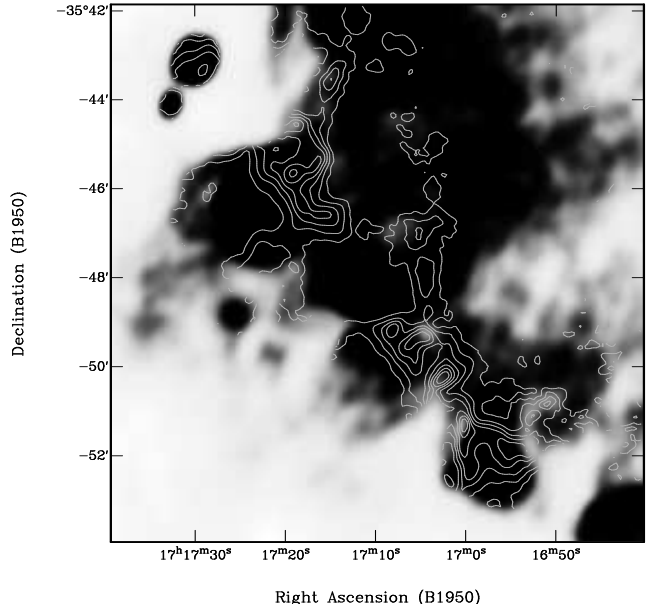
**Figure 7.** Line profiles of OH maser emission detected towards NGC 6334-V (a, b), NGC 6334-A (c, d) and NGC 6334-F (e–g). The frequencies are labelled in MHz.

towards other nearby H II regions (e.g. Whiteoak & Gardner 1974) and is believed to originate in an extended overlying foreground cloud.

3.3.1 Distribution of extended 1667-MHz OH absorption

Except at high optical depths, the line-to-continuum ratio, T_{1667}/T_c , is related to OH column densities, and can be used to investigate the large-scale spatial distribution of the OH cloud across NGC 6334. However, the interpretation of the results can be confused by the presence of either maser emission or continuum emission located in front of the OH gas.

Fig. 8. shows the peak T_{1667}/T_c distribution superimposed on continuum emission brighter than 45 mJy beam^{-1} (five times the rms noise level). Strong maser emission towards NGC 6334-F and NGC 6334-V inhibits meaningful values for these regions. The OH cloud is concentrated towards NGC 6334-A and -E and it appears to be offset to the northwest of NGC 6334-C and, to a lesser extent, NGC 6334-D. Although the results suggest that the OH column

**Figure 8.** T_{1667}/T_c contours overlaid on the 1.6-GHz continuum emission both derived with a $25.8 \times 19.6 \text{ arcsec}^2$ beam. The T_{1667}/T_c is averaged over -4.0 to -1.9 km s^{-1} . The contour levels are $-0.88, -0.75, -0.63, -0.50, -0.375, -0.25, -0.125$. The grey-scale continuum has been cut off at 45 mJy beam^{-1} .

density in front of these two continuum components is low, it may be that the bulk of the cloud extends behind them.

The south-eastern edge of this OH cloud coincides with a sharp edge of the dark dust lane mentioned previously, supporting a mixing of gas and dust. High line-to-continuum values occur in localised regions of approximately 30 arcsec in diameter within the OH concentration which extends northeast of NGC 6334-A and southwest of NGC 6334-C. The highest line-to-continuum value of -0.9 occurs at a velocity of -2.6 km s^{-1} towards $\text{RA(B1950)} = 17^h 17^m 02.5$, $\text{Dec(B1950)} = -35^{\circ} 50' 14''$. The compression of the radio continuum emission at the southern edge of NGC 6334-C (see Fig. 4) may be a result of an interaction with the OH cloud.

3.3.2 Non-LTE behaviour and the OH Sum Rule

Fig. 9 shows the line profiles towards NGC 6334-A, -E and -D at the positions that are listed in Table 3. The rms noise

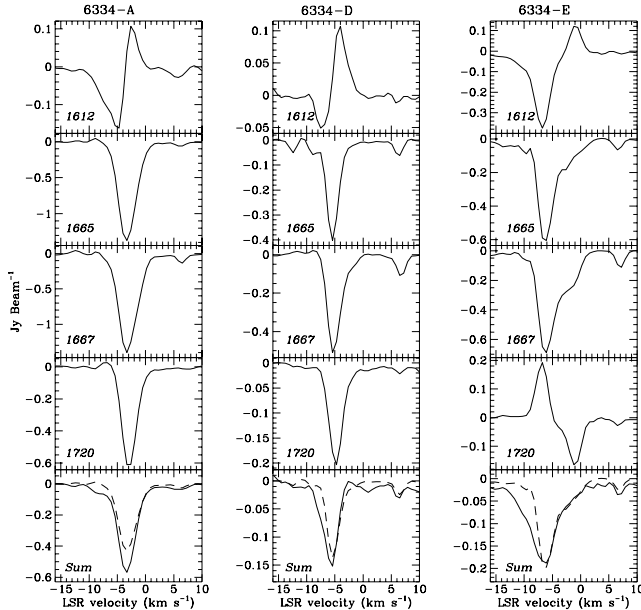


Figure 9. Line profiles of OH thermal emission and absorption towards NGC 6334-A, -D and -E. The weighted sums of the satellite lines, \sum_s (solid) and the main lines, \sum_m (dashed) are also shown.

level for each transition is less than 0.01 Jy beam $^{-1}$. Also shown are the profiles of the weighted sums \sum_s (solid) and \sum_m (dashed), defined by Eq. 2. The profiles for these three sources have been selected because they are not affected by the strong maser emission associated with the other sources and they show the typical behaviour seen for the OH cloud.

The satellite-line profiles show specific examples of the conjugate behaviour mentioned in Section 1. In addition, some profiles exhibit a ‘flip’ from emission to absorption with a change in velocity. This flip, first detected in an individual feature by Caswell & Robinson (1974) has been discussed in some detail in recent studies (e.g. Frayer, Seaquist, & Frail 1998; van Langevelde et al. 1995). An interpretation is that the more negative-velocity gas, which shows 1612-MHz absorption, has OH column densities such that $N_{OH}/\Delta V \leq 10^{15} \text{ cm}^{-2} \text{ km}^{-1} \text{ s}$ where ΔV is the full-width at half maximum of the absorption profile. For the more positive-velocity gas, which shows 1612-MHz emission, the OH column density is given by $N_{OH}/\Delta V \geq 10^{15} \text{ cm}^{-2} \text{ km}^{-1} \text{ s}$. The velocity at which this flip occurs represents the transitional density, $N_{OH}/\Delta V \approx 10^{15} \text{ cm}^{-2} \text{ km}^{-1} \text{ s}$. For the OH main-line absorption profiles in NGC 6334, $\Delta V \approx 3 \text{ km s}^{-1}$. Using the constant OH/H₂ abundance ratio of 10^{-7} (Langer & Graedel 1989), the corresponding transitional H₂ column density is $3 \times 10^{22} \text{ cm}^{-2}$.

Table 3 lists values of the peak line-to-continuum ratio measured at specific positions for all four transitions. The rms noise level in both the continuum and line images introduced an uncertainty for each measurement that was below 10 per cent. In cases where the profiles ‘flip’ from emission to absorption, the peak with the highest absolute value was used. The velocities taken from the 1665-MHz absorption and 1612-MHz emission are most positive (-2.2 km s^{-1}) just south of NGC 6334-C, become more negative towards both ends of the continuum ridge, and reach values

of -6.1 km s^{-1} towards NGC 6334-V and -8.2 km s^{-1} towards NGC 6334-F. This velocity trend is supported by the velocity trends of the OH masers (see Table 2) and has been detected in observations of other molecules (e.g. Kraemer & Jackson 1999). The trend is also present in the limited H II velocities available.

For NGC 6334-D and -E, Eq. 2 is approximately satisfied suggesting that the OH optical depths towards these regions are low. Therefore the 1665- and 1667-MHz line-to-continuum values of these two regions are valid approximations of the actual optical depths at each transition. For NGC 6334-A the sum of the line-to-continuum ratios for the satellite lines (0.58 ± 0.02) is higher than the weighted sum for the main lines (0.44 ± 0.02). This discrepancy is consistent with higher optical depths and therefore the line-to-continuum measurements as approximations of optical depth should be used conservatively.

In all measurable cases, the main-line profiles also show non-LTE line ratios. The T_{1667}/T_{1665} ratios range from 1.0 to 1.2. These values differ significantly from the LTE value of 1.8. Since we know from the results of Eq. 2 that the optical depths are low towards NGC 6334-D and -E, the non-LTE ratios for these two regions can only be explained in terms of high optical depth if the cloud is clumping on smaller scales.

3.3.3 Use of the satellite lines to probe individual OH cloud cores

Figs 10 to 12 show the velocity maps of the 1612-MHz emission and absorption for NGC 6334-V, -A, and -D. The velocity increment of each image is 0.7 km s^{-1} . Only the 1612-MHz transition is shown because the corresponding 1720-MHz transition has a similar distribution and does not demonstrate the flip from emission to absorption as clearly as the 1612-MHz transition. In all cases there is significant 1612-MHz emission which presumably results from radiative excitation of dense OH (H₂ column densities $\geq 5 \times 10^{22} \text{ cm}^{-2}$) by nearby infrared objects.

NGC 6334-V: The set of velocity maps (Fig. 10) show 1612-MHz emission present over a velocity range of -11 km s^{-1} to -2 km s^{-1} . The distribution does not mirror the continuum emission shown in Fig. 2, but consists of a concentration which extends over 2.5 arcmin in the north-south direction and 2 arcmin east-west, covering the region of enhanced infrared emission as might be expected. The distribution coincides with a region of CO(2-1) emission (Kraemer, Jackson, & Lane 1998). The possible sites of triggered star formation detected by Straw, Hyland, & McGregor (1989) trace an arc around the eastern edge of the 1612-MHz emission. The change of this emission with velocity suggests an expanding filled-shell structure. At some velocities a relatively sharp decrease in intensity is present at the south-western edge of the peak emission. The 1720-MHz OH transition is in absorption over the same velocity range as the 1612-MHz transition, and has the same distribution. To the west of the main 1612-MHz emission is an area of faint absorption. It is associated with faint 1720-MHz emission, and here, away from the infrared emission, collisional excitation may be responsible.

Although the extended main-line OH absorption is masked

Table 3. Parameters derived from the absorption and emission profiles at selected positions within NGC 6334.

Region	Position		Velocity (km s ⁻¹)	$\frac{T_{1612}}{T_c}$	$\frac{T_{1665}}{T_c}$	$\frac{T_{1667}}{T_c}$	$\frac{T_{1720}}{T_c}$	$\frac{T_{1667}}{T_{1665}}$	\sum_m^a (Jy beam ⁻¹)	\sum_s^a
	RA(B1950)	DEC(B1950)								
NGC 6334-V	17 ^h 16 ^m 35 ^s .48	-35°55'17"2	-6.1 ^b	+1.5	—	—	-0.7	—	—	—
NGC 6334-A	17 16 58.33	-35 51 38.0	-3.8 ^c	-0.1	-0.84	-0.83	-0.40	0.99 ± 0.03	0.44	0.58
NGC 6334-C	17 17 09.75	-35 49 06.0	-2.1 ^c	-0.17	-0.36	-0.36	< ±0.02	1.0 ± 0.4	—	—
NGC 6334-D	17 17 22.16	-35 46 06.6	-5.4 ^c	+0.09	-0.30	-0.37	-0.14	1.22 ± 0.09	0.19	0.18
NGC 6334-E	17 17 29.13	-35 43 09.7	-6.1 ^c	-0.28	-0.48	-0.47	-0.18	0.98 ± 0.06	0.17	0.15
NGC 6334-F	17 17 32.32	-35 44 03.9	-8.2 ^b	+0.55	—	—	—	—	—	—

^a Values of the weighted sums defined by Eq. 2 to within an error of ±0.02

^b Velocity of T_{1612} intensity peak to within an error of ±0.4 km s⁻¹. No main-line extended emission or absorption measurements can be made towards NGC 6334-V and -F because of the strong maser emission at these transitions.

^c Velocity of T_{1665} intensity peak to within an error ±0.4 km s⁻¹

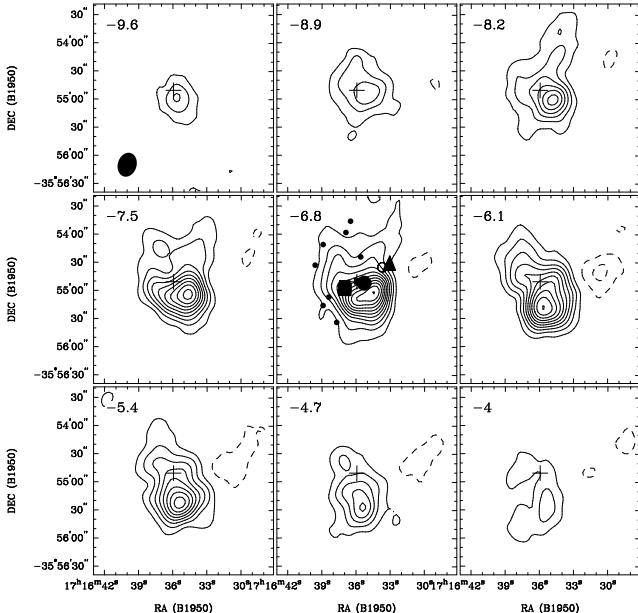


Figure 10. NGC 6334-V: 1612-GHz emission (bold) and absorption (dashed) distribution imaged with a 25.8 × 19.6 arcsec² beam, shown bottom left. The contour levels are -50, -25, 25, 50, 75, 100, 125, 150, 175, 200, 225, 250 and 275 mJy beam⁻¹. The sites of OH masers (cross) are shown on all images. The other symbols are described in the caption of Fig. 2

by two bright masers (see Fig. 7), a comparison of peak line-to-continuum ratios at 1612 MHz and 1720 MHz, listed in Table 3, indicates anomalous behaviour. The average of the two values (+0.4) is positive, whereas for a simple OH-absorption environment the Sum Rule decrees that the value must be negative. One explanation might be that radiative excitation of a dense OH cloud by the embedded infrared objects has resulted in low-gain maser amplification at 1612 MHz.

NGC 6334-A: The profiles in Fig. 9 show, 1612-MHz absorption between -8 and -6 km s⁻¹ and then 1612-MHz emission to +1 km s⁻¹. At 1720 MHz, emission between -10 and -5 km s⁻¹ is followed by deep absorption extending to +1 km s⁻¹. The weighted-sum profile has a shape similar to the main-line profiles, as predicted by the Sum Rule. Con-

jugate satellite-line behaviour is obviously present and the extent is given by the deviations of the individual spectra from the weighted-sum profile. Accordingly, for the 1612-MHz transition, the deviations would show a profile similar in shape to the 1612-MHz emission profile, but the absorption intensity would be reduced and emission intensity increased (to about 0.2 Jy beam⁻¹). For the 1720-MHz transition the difference spectrum would show exact conjugate behaviour.

The set of velocity maps (Fig. 11) show that the overall distribution of the 1612-MHz absorption and emission is spherical, with an average diameter of about 1 arcmin, and coincides with the central region of bright continuum emission in Fig. 3. The extent is similar to that for the NH₃ emission (Kraemer et al. 1997). At a velocity of -4 km s⁻¹ the distribution splits into absorption and emission components, diametrically offset. At the extreme velocities, the relative offset virtually disappears, ruling out rotation. The 1720-MHz transition exhibits conjugate behaviour with the same distribution as the 1612-MHz transition, including the splitting at -4 km s⁻¹.

The results are consistent with satellite-line anomalies resulting from OH excitation by the infrared objects embedded in the cloud and a density gradient that increases with the more positive observed velocities of the molecular gas. This density gradient may also explain the distribution at a velocity of -4 km s⁻¹ and is discussed further in Section 4.2.

NGC 6334-D: For the 1612-MHz transition, the profiles in Fig. 9 show absorption from -10 km s⁻¹ to -5 km s⁻¹ then emission extending to 0 km s⁻¹. The 1720-MHz transition is totally in absorption. Comparison of these profiles with the weighted-sum profile suggests that anomalous satellite-line behaviour is present only at velocities more positive than -7 km s⁻¹. Here, the enhanced 1612-MHz emission is accompanied by enhanced 1720-MHz absorption.

The set of velocity maps (Fig. 12) reveal that the distribution of the 1612-MHz absorption and emission is not completely coincident with the region of brightest continuum emission. Instead of an approximately spherical distribution centred near IRS-24, 1612-MHz emission is concentrated along an arc to the west of the object. The 1720-MHz absorption was found to have a similar distribution. The offset locations are consistent with the extended OH cloud distri-

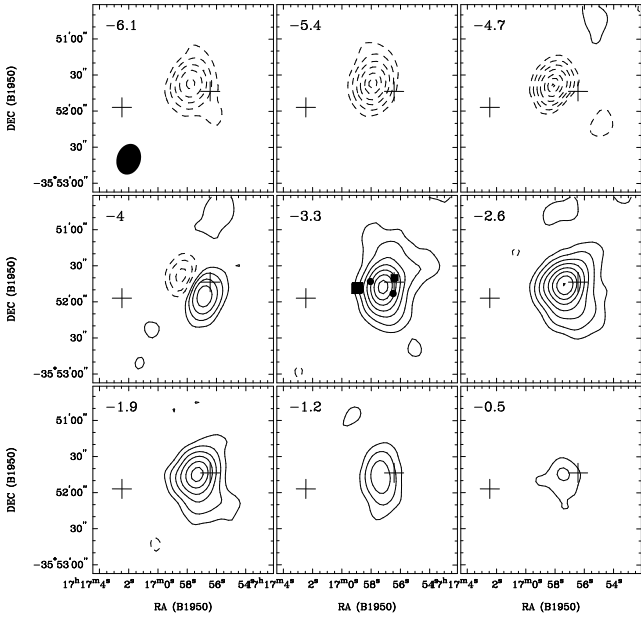


Figure 11. NGC 6334-A: 1612-GHz emission (bold) and absorption (dashed) distribution imaged with a 25.8×19.6 arcsec 2 beam, shown bottom left. The contour levels are $-235, -210, -175, -125, -85, -50, -25, 25, 50, 85, 125, 175, 225, 275, 325$ mJy beam $^{-1}$. The sites of the OH masers (cross) are shown on all images. The other symbols are described in the caption of Fig. 3.

bution traced by the 1667-MHz absorption in Fig. 8. There are no velocity trends to confirm the presence of a possible outflow in the region. The anomalous satellite-line behaviour is presumably due to the OH excitation by one or more of the infrared sources. It may be significant that for both this and the previous case, the H α velocities fall within the velocity range of the 1612-MHz emission.

NGC 6334-E: Anomalous satellite behaviour dominates the 1612-MHz and the 1720-MHz profiles shown in Fig. 9. The 1612-MHz absorption from -12 km s $^{-1}$ to -4 km s $^{-1}$ followed by emission to $+1$ km s $^{-1}$ is matched by a conjugate variation at 1720 MHz. This is a typical example of the anomaly flip discussed in Section 3.3.1, and the results can be interpreted in terms of low-density gas for the more negative observed velocities and high-density for the more positive observed velocities. The distribution of the absorption and emission at 1612 and 1720 MHz follows the 1.6-GHz continuum emission (see Fig. 6) and is consistent with an overlying OH cloud.

NGC 6334-F: Information about the extended OH is very restricted because the main-line and 1720-MHz observations are dominated by bright maser emission (see Fig. 7). The 1612-MHz transition is also in emission centred near the continuum emission peak, at RA(B1950) = $17^h 17^m 32.42 \pm 0.01$, Dec(B1950) = $-35^{\circ} 44' 05.4 \pm 0.1$. The narrow velocity width of 1.8 km s $^{-1}$ and the unresolved angular size would be consistent with maser emission. However the peak intensity of 0.19 Jy beam $^{-1}$ is at least two orders of magnitude lower than the intensities of the other masers. In addition, the position differs by 1.8 arcsec from the position of the other masers and the velocity of the peak (-8.2 km s $^{-1}$) is more positive than the velocities of the 1720-MHz and main-line masers (-8.9 and -10.2 km s $^{-1}$ respectively). Interpretation

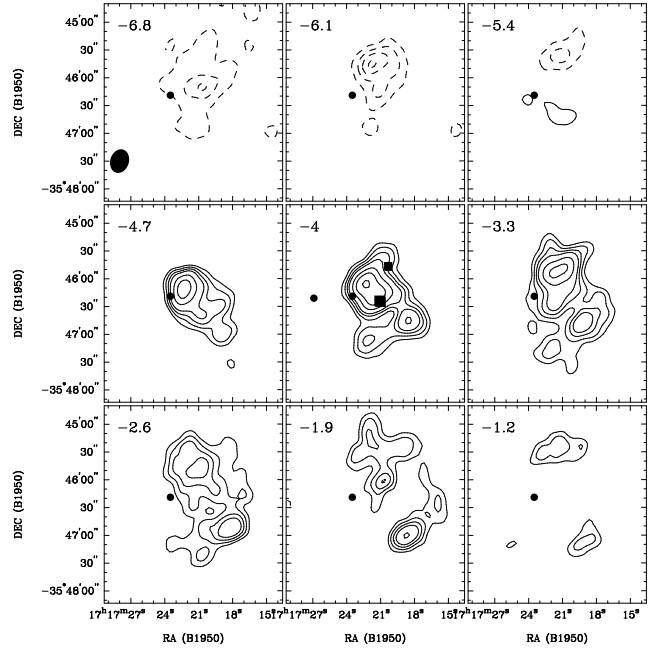


Figure 12. NGC 6334-D: 1612-GHz emission (bold) and absorption (dashed) distribution imaged with a 25.8×19.6 arcsec 2 beam, shown bottom left. The contour levels are $-100, -75, -50, -25, 30, 40, 50, 60, 80, 100, 125, 150, 175, 200, 225, 250$ and 275 mJy beam $^{-1}$. IRS-24 (small circle) is shown on all images. The other symbols are described in the caption of Fig. 5.

of the results is difficult without additional information. The presence of several infrared objects and masers (see Fig. 6) suggest a region of considerable star-forming activity. Excitation of a high-density OH cloud by infrared radiation could be responsible for the 1612-MHz emission and possibly the other OH masers. On the other hand, the intensity of the 1720-MHz and the absence of 1612-MHz absorption may indicate that collisional excitation is predominant.

4 DISCUSSION

4.1 Overall cloud structure

The OH velocity and line-to-continuum trends support a bar-like shape for the molecular cloud/dust complex in the following manner. The cloud may wrap behind NGC 6334-C (or disappear) and then curve forward towards NGC 6334-E and NGC 6334-A. This shape was first put forward by Moran & Rodríguez (1980). They used the sequential theory of Elmegreen & Lada (1977) to suggest that star formation in the molecular cloud may have been triggered by an OB association located behind it. If the cloud were shaped like a tube which is bent away from the OB association (resulting in more negative velocities towards the ends) then a shock wave traveling from the OB association would hit the central part of the cloud first and then move outwards towards each end. This model was initially used to explain why the active sites of star-formation (NGC 6334-V and -F) are located at the end of the molecular cloud and the more evolved regions (NGC 6334-C and -D) nearer the centre. However, this model has been complicated by evidence of ongoing star-formation, such as infrared sources, outflows and OH maser

emission (this paper) towards the central continuum concentrations. Perhaps a burst of secondary star formation had begun in these regions.

As stated previously, the line-to-continuum ratio is related to OH column densities but interpretation of the results can be confused if the continuum emission is located in front of the absorbing gas, which may be the case for NGC 6334-C and D. In regions where the OH gas appears to be concentrated near the edges of the continuum emission, the OH may be gradually becoming dissociated by the expanding ionized regions or used up for star formation. The column density of the extended molecular cloud increases towards each end of the continuum axis. This could result from the increased line-of-sight path-length at the ends of the forward-curving molecular cloud. Alternatively, it would be consistent with a gas supply not yet dissipated by existing H II regions or used up in star formation. If NGC 6334-C were more evolved than the other sources, it is feasible that the surrounding molecular cloud would be dissociated first.

4.2 Satellite-line anomalies

Several cases of flips across the satellite-line profiles have been identified and they have been interpreted as a density gradient. There are no complete models which can explain these flips astrophysically. To explain their presence in our data, we suggest a simple model whereby an H II concentration is located behind a more extended OH cloud. The OH cloud has a velocity range of -15 to $+2 \text{ km s}^{-1}$ and consists of a low density layer, producing 1612-MHz absorption, and an adjacent high density layer, producing 1612-MHz emission. The transitional density is given by $N_{\text{OH}} \approx 10^{15} \Delta V \text{ km}^{-1} \text{ s cm}^{-2}$. The high density layer, with velocities of -6 to $+2 \text{ km s}^{-1}$ and which also include the H II velocities, is nearer the H II region and the low density layer, with velocities of -15 to -4 km s^{-1} , is further out along the line of sight.

The adjacent 1612-MHz emission and absorption observed at the transitional velocity in NGC 6334-A (-4 km s^{-1} of Fig. 11) may be explained if the direction of the density gradient within the OH cloud differs from the direction of the velocity gradient, and that isovelocity planes do not coincide with isodensity planes. The angle of deviation may be large enough so that at the transitional velocity it is possible to observe the low density gas on one side of the continuum emission and the high density gas on the other.

5 CONCLUSION

We have imaged the 1.6-GHz continuum and the four transitions of the $^2\Pi_{3/2}$, $J=3/2$ ground state of OH towards the NGC 6334 H II region/molecular cloud complex. Observations were made with the Australia Telescope Compact Array with angular resolutions of $4.6 \times 7.2 \text{ arcsec}^2$ and $25.8 \times 19.6 \text{ arcsec}^2$. The results are as follows:

(a) *1.6-GHz Continuum distribution* - The continuum emission has been detected over an area of $35 \times 25 \text{ arcmin}^2$. The main region shows a set of aligned concentrations in stages of evolution ranging from compact regions to well-evolved shells. They are superimposed on a faint extended

area. Two additional southern regions appear as extended incomplete shells.

(b) *OH maser emission* - We have detected seven masers, plus a possible faint maser candidate. Including the eighth possible maser, the masers are present for all OH transitions and appear to be associated with the continuum concentrations. Two of the masers were detected towards NGC 6334-A. All maser locations include main-line transitions. The maser velocities vary between -8.7 and 0.5 km s^{-1} , with the more positive velocities located near the centre of the continuum distribution.

(c) *Extended OH distribution* - Main-line OH absorption was detected towards almost all of the continuum emission. The distribution of the line-to-continuum ratio at 1667-MHz ratio is uniform across the continuum and varies between -0.4 and -0.9 . The distribution is not enhanced towards the continuum emission but is concentrated in a bar extending northeast-southwest with its sharp south-eastern edge coincident with that of the optical dust lane. Our velocity and line-to-continuum results support the notion in which the molecular bar wraps around the continuum emission.

(d) *Non-LTE behaviour*

For the satellite lines, one transition is commonly in emission with the other simultaneously in absorption. The 1612-MHz transition is in emission near the prominent radio continuum concentrations, presumably reflecting OH excitation by the infrared radiation associated with these concentrations. In some cases, the conjugate-type behaviour is observed to reverse across a spectral-line profile. This has been interpreted as a density gradient, and we have suggested that this reflects the presence of different cloud regimes along a line of sight. The main-line transitions show non-LTE behaviour in that the T_{1667}/T_{1665} intensity ratios range from 1.0 to 1.2, significantly lower than the LTE value of 1.8. The results of the OH Sum Rule suggest that this discrepancy can only be explained in terms of high optical depth if the cloud is clumping on smaller scales.

ACKNOWLEDGMENTS

We thank Neil Killeen and Bob Sault for assistance with the data reduction and analysis and John Storey and Jochen Liske for valuable discussions. We also thank Jim Caswell and the referee for providing some very helpful comments. KJB acknowledges the support of an Australian Post-graduate Award.

REFERENCES

- Bachiller R., Cernicharo J., 1990, A&A, 239, 276
- Caswell J. L., 1997, MNRAS, 289, 203
- Caswell J. L., 1998, MNRAS, 297, 215
- Caswell J. L., Robinson B. J., 1974, Aust. J. Phys, 27, 597
- Cheung L., Frogel J. A., Gezari D. Y., Hauser M. G., 1978, ApJ, 226, L146
- De Pree C. G., Rodríguez L. F., Dickel H. R., Goss W. M., 1995, ApJ, 447, 220
- Dickel H. R., Dickel J. R., Wilson W. J., 1977, ApJ, 217, 56
- Elitzur M., 1992, Astronomical masers. Kluwer Academic Publishers, Dordrecht
- Ellingsen S. P., Norris R. P., McCulloch P. M., 1996, MNRAS, 279, 101

Elmegreen B. G., Lada C. J., 1977, *ApJ*, 214, 725

Fischer J., Joyce R. R., Simon M., Simon T., 1982, *ApJ*, 258, 165

Fischer J., Saunders D. B., Simon M., Solomon P. M., 1985, *ApJ*, 293, 508

Forster J. R., Caswell J. L., 1989, *A&A*, 213, 339

Frater R. H., Brooks J. W., 1992, *Electr. Electron. Eng. Aust.*, 12, 103

Frayer D. T., Seaquist E. R., Frail D. A., 1998, *AJ*, 115, 559

Gardner F. F., Whiteoak J. B., 1975, *MNRAS*, 173, 131

Gaume R. A., Mutel R. L., 1987, *ApJS*, 65, 193

Gooch R., 1996, in Jacoby G. H., Barnes J., ed, *Astronomical Data Analysis Software and Systems V*, Vol. 101. ASP Conference Series, San Francisco, p. 80

Harvey P. M., Gatley I., 1983, *ApJ*, 269, 613

Jackson J. M., Kraemer K. E., 1999, *ApJ*, 512, 260

Kraemer K. E., Jackson J. M., 1995, *ApJ*, 439, L9

Kraemer K. E., Jackson J. M., 1999, *ApJS*, 124, 439

Kraemer K. E., Jackson J. M., Lane A. P., 1998, *ApJ*, 503, 785

Kraemer K. E., Jackson J. M., Paglione T. A. D., Bolatto A. D., 1997, *ApJ*, 478, 614

Langer W. D., Graedel T. E., 1989, *ApJ*, 61, 241

McBreen B., Fazio G. G., Stier M., Wright E. L., 1979, *ApJ*, 232, L183

Moran J. M., Greene B., Rodríguez L. F., Backer D. C., 1990, *ApJ*, 348, 147

Moran J. M., Rodríguez L. F., 1980, *ApJ*, 236, L159

Neckel T., 1978, *A&A*, 69, 51

Persi P., Ferrari-Toniolo M., 1982, *A&A*, 112, 292

Persi P., Roth M., Tapia M., Marenzi A. R., Felli M., Testi L., Ferrari-Toniolo M., 1996, *A&A*, 307, 591

Persi P., Tapia M., Felli M., Lagage P. O., Ferrari-Toniolo M., 1998, *A&A*, 336, 1024

Reifenstein E. C., Wilson T. L., Burke B. F., Mezger P. G., Altenhoff W. J., 1970, *A&A*, 4, 357

Rodríguez L. F., Cantó J., Moran J. M., 1982, *ApJ*, 255, 103

Rodríguez L. F., Cantó J., Moran J. M., 1988, *ApJ*, 333, 801

Rogers A. E., Barrett A. H., 1967, in van Woerden H., ed, *Radio Astronomy and the Galactic System*, Vol. 31. I.A.U. Symposium, London, p. 77

Sault R. J., Teuben P. J., Wright M. C. H., 1995, in Shaw R., Payne H., Hayes J., ed, *Astronomical Data Analysis Software and Systems IV*, Vol. 77. ASP Conference Series, San Francisco, p. 433

Sault R. J., Wieringa M. H., 1994, *A&AS*, 108, 585

Schraml J., Mezger P. G., 1969, *ApJ*, 156, 269

Steer D. G., Dewdney P. E., Ito M. R., 1984, *A&A*, 137, 159

Straw S. M., Hyland A. R., 1989a, *ApJ*, 347, 876

Straw S. M., Hyland A. R., 1989b, *ApJ*, 340, 318

Straw S. M., Hyland A. R., McGregor P. J., 1989, *ApJS*, 69, 99

Tapia M., Persi P., Roth M., 1996, *A&A*, 316, 102

van Langevelde H. J., van Dishoeck E. F., Sevenster M. N., Israel F. P., 1995, *ApJ*, 448, L123

Whiteoak J. B., Gardner F. F., 1974, *A&A*, 37, 389

Wolstencroft R. D., Scarrott S. M., Warren-Smith R. F., 1987, *MNRAS*, 228, 805